THE JOURNAL OF PHYSICAL CHEMISTRY C
A JOURNAL OF THE AMERICAN CHEMICAL SOCIETY

pubs.acs.org/JPCC

Article

The Influence of Pd-Atom Substitution on $Au_{25}(SC_8H_9)_{18}$ Cluster Photoluminescence

Patrick J. Herbert, Marcus A. Tofanelli, Christopher J. Ackerson, and Kenneth L. Knappenberger, Jr.*

Cite This: *J. Phys. Chem. C* 2021, 125, 7267–7275

Read Online

ACCESS | Metrics & More | Article Recommendations

ABSTRACT: The photoluminescence (PL) of $Au_{25}(SC_8H_9)_{18}$ and $Au_{24}Pd(SC_8H_9)_{18}$ was investigated using variable-field magnetic circular photoluminescence (VH-MCPL) spectroscopy. The comparison of low-temperature (4.5 K) PL spectra measured for both nanoclusters revealed an ≈40 meV blueshift of intraband emission upon Pd substitution. Compared to that for the the $Au_{25}(SC_8H_9)_{18}$ cluster, the degree of circular-polarization for the $Au_{24}Pd(SC_8H_9)_{18}$ cluster increased for the low energy (<1.65 eV) portion of the PL spectrum, but decreased for the higher energy (>1.65 eV) spectral region. MCPL spectra included three distinct components, underlying the global PL spectrum, for both clusters. Variable-field analysis of each MCPL component revealed an increase in spin−orbit coupling (Landé g-factor) magnitudes for radiative transitions of the Pd-substituted cluster with respect to $Au_{25}(SC_8H_9)_{18}$. Variable-temperature (VT) PL spectroscopy yielded reduced integrated global PL intensity and increased electron-vibrational coupling for $Au_{24}Pd(SC_8H_9)_{18}$, as compared to $Au_{25}(SC_8H_9)_{18}$. The results indicate that Pd-substitution for Au in $Au_{25}(SC_8H_9)_{18}$ results in increased angular momenta for metal−metal intraband transitions; the Landé g-factor for these transitions increased by ≈55% upon substitution, as compared to an approximate 19% increase for ligand-based transitions. The increased angular momentum translates to a 30% increase in electron−phonon coupling constants for intraband transitions, but only a 3% increase for ligand-based transitions. As a result, Pd substitution leads to less efficient metal−metal (intraband) radiative emission for $Au_{24}Pd(SC_8H_9)_{18}$ than for $Au_{25}(SC_8H_9)_{18}$.

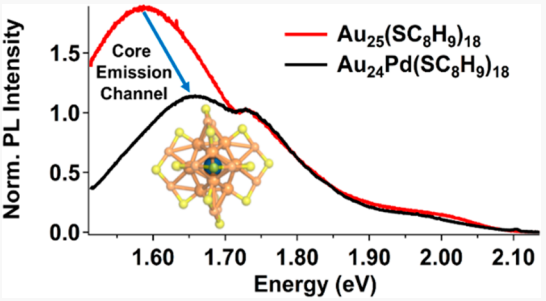

INTRODUCTION

Owing to adaptable colloidal synthesis, monolayer-protected clusters (MPCs) serve as structurally well-defined prototypes for understanding photonic metals.[1−4] The $Au_{25}(SC_8H_9)_{18}$ MPC, in which $-SC_8H_9$ represents phenylethanethiol (PET), has widely served as a model system for deriving structure−function relationships of metal clusters.[5,6] The $Au_{25}(SC_8H_9)_{18}$ cluster is characterized by three structural domains: (1) a core comprising metal atoms; (2) an organometallic layer of alternating metal−chalcogenide "staple" units or metal−phosphine linkages; and (3) a passivating layer of organic ligands that serve to stabilize the cluster in solution.[7−10] Advances in synthesis and purifications have enabled isolation of clusters with structural modifications addressable to each domain.[10−12] In particular, synthesis and characterization of multimetal clusters has been shown to be an effective route to modulate optical properties.[12−16] For $Au_{25}(SC_8H_9)_{18}$, three metal substitution positions can be defined: (1) the center position of the 13-atom icosahedral core, (2) outer surface sites of the core, and (3) metal sites within the staple units.[17] Selective substitution positions have been identified for a variety of transition metals,[18] thus providing predictive synthetic routes to achieve site-specific metal atom substitution to form bi-, tri-, and tetra-metal $Au_{25}(SR)_{18}$ derivatives.[18,19] These metal substitutions have resulted in changes in photoluminescence (PL) emission yields and photocatalytic efficiencies.[14,20,21]

Metal substitution also affects MPC electron configuration, spin polarization, and carrier dynamics.[22−29] Electrochemical modifications allow similar types of effects.[29−32] For many MPCs, including $Au_{25}(SC_8H_9)_{18}$, electron configurations can be predicted using superatom models adapted from gas-phase metal clusters.[33] For superatoms, the valence electron(s) contributed by each metal atom are treated as delocalized over the spherically approximated core.[33] Total valence electron counts that result in a closed shell configuration (i.e., 2, 8, 18, etc.) are expected to result in stable clusters.[33,34] For MPCs, consideration of electron withdrawing ligands and cluster oxidation state formulate the total electron count as $n^* = N - M - z$ where N is the total valence electrons, M is the number of ligands, and z is the oxidation state.[35] For the anionic and cationic $Au_{25}(SC_8H_9)_{18}^{-,+}$ clusters, superatom electron counts

Received: January 29, 2021
Revised: March 12, 2021
Published: March 26, 2021

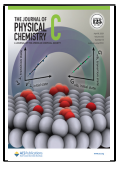

https://doi.org/10.1021/acs.jpcc.1c00799
J. Phys. Chem. C 2021, 125, 7267−7275

result in spin-paired $1S^21P^6$ and $1S^21P^4$ configurations, respectively.[35] Conversely, the neutral $Au_{25}(SC_8H_9)_{18}^0$ cluster is predicted to have an open shell $1S^21P^5$ configuration.[35] Electron paramagnetic resonance (EPR) and superconducting quantum interference device (SQUID) magnetic susceptibility studies observed diamagnetic behavior for the $Au_{25}(SC_8H_9)_{18}^{-,+}$ clusters, whereas paramagnetic character was observed for the neutral cluster.[30,32] Recently, oxidation-dependent femtosecond time-resolved circularly polarized transient absorption (fs-CPTA) spectroscopic measurements of the $Au_{25}(SC_8H_9)_{18}$ cluster revealed picosecond spin-conversion dynamics for the open-shell neutral species.[29] No spin-conversion dynamics were observed for the closed-shell anionic and cationic clusters.[29] This spin conversion results in spin-polarized emission by paramagnetic $Au_{25}(SC_8H_9)_{18}$.[36] Control over the MPCs spin configurations through electrochemical modification of the superatom electron counts is a promising avenue toward magnetic and spintronic applications.[26,29−31,37]

Substitution of nonisoelectronic metals into the MPC core also alters superatom electron counts.[22,23,25,29] One example is the $Au_{24}Pd(SR)_{18}$ cluster.[22,38] Theoretical electronic structure calculations of $Au_{24}Pd(SR)_{18}$ cluster isomers predict the preferential substitution of Pd at the center position of the 13-atom icosahedral core.[39−41] The assignment of preferential substitution of Pd to the center position is supported by ^{197}Au Mössbauer, X-ray absorption fine structure (EXAFS), and single-crystal X-ray diffraction analyses.[22,42,43] Static substitution disorder refinement analysis of the $Au_{24}Pd(SC_8H_9)_{18}$ crystal structure determined 92.6% occupancy of Pd at the core center position.[22] Single-Pd-atom substitution of the $Au_{25}(SR)_{18}$ cluster core can modify superatom electron configurations similarly to electrochemical methods.[22,29] Because of the $4d^{10}$ valence electron configuration of Pd, no electrons are expected to contribute to the superatom electron count.[22,25,29,38−40] This is expected to render the $Au_{24}Pd(SC_8H_9)_{18}$ cluster as a six-electron superatom system, and isoelectronic with the cationic $Au_{25}(SC_8H_9)_{18}^+$ cluster.[22,25,29,38−40] Cyclic voltammetry and EPR studies on the $Au_{25}(SC_8H_9)_{18}^q$, where q = −1, 0, +1, and $Au_{24}Pd(SC_8H_9)_{18}$ clusters support this assignment.[30,32] In addition, analysis of fs-CPTA measurements of $Au_{24}Pd(SC_8H_9)_{18}$ by Williams et al. similarly reported no observed spin conversion dynamics for the $Au_{24}Pd(SC_8H_9)_{18}$ cluster.[29] Previously, fsTA studies of $Au_{24}M(SC_8H_9)_{18}$, where M = Pd, Pt, reported accelerated carrier dynamics upon metal substitution.[28] This observation suggests that metal substitution can influence carrier relaxation pathways, along with modifying spin-configurations.

Here, the transient electronic structure and emission properties of $Au_{24}Pd(SC_8H_9)_{18}$ are compared to $Au_{25}(SC_8H_9)_{18}$, based on results from variable-field magnetic circular photoluminescence ($V\vec{H}$-MCPL) and variable-temperature (VT) PL spectroscopy. $V\vec{H}$ methods have been effectively used to describe metal−metal and metal-to-ligand transitions in clusters ranging from $Au_{25}(SC_8H_9)_{18}$ to $Au_{102}(pMBA)_{44}$.[36,44−46] Comparison of linear absorption and low-temperature (4.5 K) PL spectra measured for $Au_{25}(SC_8H_9)_{18}$ and $Au_{24}Pd(SC_8H_9)_{18}$ revealed an observable blueshift for HOMO−LUMO transitions for the Pd-substituted cluster. This blue shift resulted from differences in cluster electron valency.[7,47,48] The MCPL spectra were qualitatively similar for both clusters, consisting of three distinguishable emission components. Compared to the $Au_{25}(SC_8H_9)_{18}$ cluster, $Au_{24}Pd(SC_8H_9)_{18}$ exhibited a larger degree of circular-polarization (DOCP) at lower energy (<1.65 eV), but a smaller value for larger emission energy (>1.65 eV). $V\vec{H}$-MCPL analysis revealed greater spin−orbit coupling angular momenta for all $Au_{24}Pd(SC_8H_9)_{18}$ PL components, relative to $Au_{25}(SC_8H_9)_{18}$. Electron-vibrational coupling constants were uniformly greater for $Au_{24}Pd(SC_8H_9)_{18}$. Specifically, an increase in angular momenta of approximately 55% for the metal−metal intraband emission transition was correlated to a 30% increase in the electron-vibrational coupling constant. Consequentially, more efficient intraband nonradiative decay led to reduced global PL.

MATERIALS AND METHODS

The synthetic protocol for $Au_{25}(SC_8H_9)_{18}$ and $Au_{24}Pd(SC_8H_9)_{18}$ is reported in the literature.[22,49,50] Samples were dispersed into a 17% (w/w) solution of polystyrene/toluene. The concentration of the cluster solution was approximately 600 μM. The solution was then dropcast onto a quartz coverslip and allowed to dry in a vacuum desiccator. Linear absorption spectra of the MPC film were acquired at room temperature using a Lambda 950 UV−vis spectrometer (PerkinElmer). The coverslip was then affixed with a polarization film necessary for MCPL analysis.[45] The combined MPC slide and polarization film were mounted onto a fiber optic containing probe, loaded into the bore of the 17.5 T superconducting magnet and cooled to 4.5 K. The applied field strength and sample temperatures were controlled set to values spanning from 0 to 17.5 T and 4.5−200 K, respectively. Optical excitation was achieved using the frequency-doubled output of a 1 kHz regeneratively amplified Ti:sapphire laser system centered at 1.55 eV and approximately 100 fs in duration. The frequency-doubled 3.1 eV laser pulses were attenuated to 800 nJ/pulse and aligned onto the sample. The resulting PL was collected with a fiber optic in transmission geometry. Longpass filters set at 2.3 eV were used to isolate the photoluminescence PL from the principle excitation source. Finally, the PL photons were sent to a spectrometer (McPherson) which spectrally dispersed the emission onto a liquid nitrogen cooled 1024-pixel CCD array (Princeton Instruments).

RESULTS

Comparison of Excitation Spectrum for $Au_{25}(SC_8H_9)_{18}$ and $Au_{24}Pd(SC_8H_9)_{18}$ Clusters. Figure 1a shows normalized absorption spectra collected at room temperature for $Au_{25}(SC_8H_9)_{18}$ and $Au_{24}Pd(SC_8H_9)_{18}$ dispersed in 17% (w/w) polystyrene/toluene films. Multiple spectrally convoluted absorption features are observed for both clusters. Theoretical electronic structure modeling of the $Au_{25}(SC_8H_9)_{18}$ predicts that lower energy (<2.0 eV) absorption features arise from core-based transitions.[7,47,48] Higher energy (>2.8 eV) absorption features are predicted to arise from ligand-to-core based transitions.[7,47,48] The intermediate energy region (2.0 to 2.8 eV) may arise from transitions between mixed core- and ligand-based states. The assignment of these transitions has been supported by excitation energy dependent femtosecond time-resolved transient absorption studies of $Au_{25}(SR)_{18}^x$ clusters, where -SR is a thiolate ligand derivative, and x is the oxidation state (−1, 0, +1) state.[6,29] For excitation near the HOMO−LUMO gap energy of the $Au_{25}(SC_8H_9)_{18}$ cluster, two

https://doi.org/10.1021/acs.jpcc.1c00799
J. Phys. Chem. C 2021, 125, 7267−7275

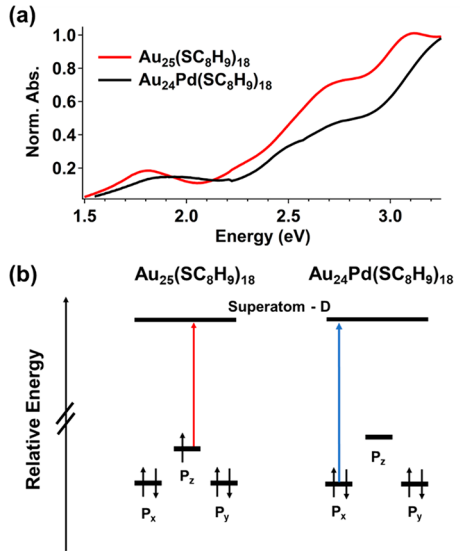

Figure 1. (a) Linear absorption spectrum for $Au_{25}(SC_8H_9)_{18}$ (red) and $Au_{24}Pd(SC_8H_{918}$ (black) dispersed in polystyrene/toluene film collected at room temperature. (b) Model for $Au_{25}(SC_8H_9)_{18}$ (left) and $Au_{24}Pd(SC_8H_9)_{18}$ (right) superatom configuration.

absorption features are observed at approximately 1.82 and 1.95 eV.[29] Theoretical electronic structure modeling has suggested that these two absorption features arise from superatom D ← P HOMO; HOMO−1 transitions.[7,47,48] Figure 1b (left) depicts the energy level diagram for $Au_{25}(SC_8H_9)_{18}$ near the HOMO−LUMO gap.[32] The energy difference between the superatom-P HOMO and HOMO−1, −2 arises from fine structure splitting of superatom orbitals due to spin−orbit coupling interactions and ligand-field effects.[45,48,51] Inspection of the absorption spectrum for the $Au_{24}Pd(SC_8H_9)_{18}$ cluster reveals energetic blue shifting of approximately 130 meV and peak broadening near the HOMO−LUMO gap excitations, relative to the $Au_{25}(SC_8H_9)_{18}$ cluster. This observed blue shift is explained by the superatom model. Because of the d^{10} valence electronic configuration of Pd, the $Au_{24}Pd$ $(SC_8H_9)_{18}$ cluster is rendered as a six electron superatom.[22,25,29,39−41] As a result, the superatom P_z orbital is no longer occupied, leaving the $P_{x,y}$ superatom orbitals as nearly degenerate HOMO;HOMO−1 states.[22,25,29,39−41] As depicted in Figure 1b (right), the unoccupation of the P_z orbital results in a larger HOMO−LUMO energy gap, and observed spectroscopic blue shifting of the first absorption peak.[22] It should be noted that this spectral blue shifting is also observed for the isoelectronic $Au_{25}(SC_8H_9)_{18}^+$ superatom cluster.[29,32]

Comparison of Photoluminescence Spectra and Spin-Polarized Emission for $Au_{25}(SC_8H_9)_{18}$ and $Au_{24}Pd(SC_8H_9)_{18}$ Clusters. Figure 2a shows the PL spectra for $Au_{25}(SC_8H_9)_{18}$ and $Au_{24}Pd$ $(SC_8H_9)_{18}$ resulting from 3.1 eV excitation at 4.5 K normalized at maximum PL amplitude for each cluster. As previously reported, the global PL spectrum for the $Au_{25}(SC_8H_9)_{18}$ cluster measured in this energy range consists of three spectrally convoluted PL components, which have been assigned to either intraband metal−metal superatom or metal-to-ligand charge transfer emission.[36,44,45,52] Inspection of the PL spectrum (Figure 2a) for the $Au_{24}Pd(SC_8H_9)_{18}$ cluster reveals a qualitatively similar spectral profile, suggesting that multiple components also contribute to PL emission. One noticeable difference in the PL spectra for the two clusters is

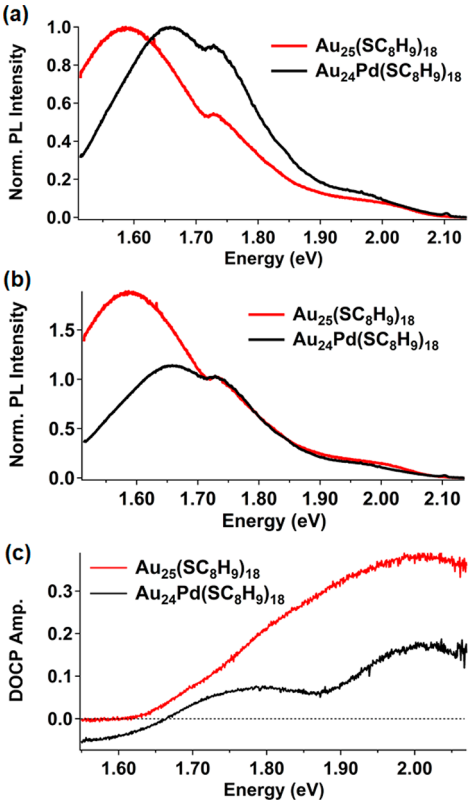

Figure 2. (a) PL spectra of $Au_{25}(SC_8H_9)_{18}$ (red) and $Au_{24}Pd$ $(SC_8H_9)_{18}$ (black) taken at 4.5 K upon 3.1 eV excitation normalized at maximum PL amplitude. The dip in the PL spectra at 1.71 eV is due to absorption by the fiber optic used for PL acquisition. (b) PL spectra of $Au_{25}(SC_8H_9)_{18}$ (red) and $Au_{24}Pd(SC_8H_9)_{18}$ (black) taken at 4.5 K upon 3.1 eV excitation normalized at 1.71 eV. (c) Degree of circular photoluminescence spectra of $Au_{25}(SC_8H_9)_{18}$ (red) and $Au_{24}Pd(SC_8H_9)_{18}$ (black) acquired at 4.5 K and 17.5 T.

that emission intensity for $Au_{24}Pd(SC_8H_9)_{18}$ is globally blue-shifted relative to the $Au_{25}(SC_8H_9)_{18}$ cluster. This PL blue shifting is consistent with the increased HOMO−LUMO energy gap for the $Au_{24}Pd(SC_8H_9)_{18}$ cluster, observed in the linear absorption spectrum (Figure 1a). However, an alternative explanation for the PL blue shift involves a different distribution of spectral weights for the PL components of $Au_{24}Pd(SC_8H_9)_{18}$ than for $Au_{25}(SC_8H_9)_{18}$. Figure 2b shows the PL spectra for $Au_{24}Pd(SC_8H_9)_{18}$ and $Au_{25}(SC_8H_9)_{18}$ normalized at 1.71 eV. The dip in spectral amplitude at 1.71 eV results from fiber absorption during PL collection. This 1.71 eV absorption is accounted for as a negative amplitude component in all fits reported here. The 1.71 eV absorption serves as a reference point of comparison for the PL spectra for $Au_{24}Pd(SC_8H_9)_{18}$ and $Au_{25}(SC_8H_9)_{18}$. The high energy (>1.71 eV) spectral profiles for $Au_{24}Pd(SC_8H_9)_{18}$ and $Au_{25}(SC_8H_9)_{18}$ clusters are relatively well overlaid. Inspection of the low energy (<1.71 eV) spectral profiles reveals lower PL amplitude for $Au_{24}Pd(SC_8H_9)_{18}$ relative to $Au_{25}(SC_8H_9)_{18}$.

To understand the effects of Pd-substitution on spin-polarized emissive relaxation, the DOCP spectrum was quantified for each cluster. Figure 2c shows the DOCP spectrum for the $Au_{25}(SC_8H_9)_{18}$ (red) and $Au_{24}Pd(SC_8H_9)_{18}$ (black) clusters acquired at 4.5 K and 17.5 T. The DOCP spectrum was determined using eq 1

https://doi.org/10.1021/acs.jpcc.1c00799
J. Phys. Chem. C 2021, 125, 7267−7275

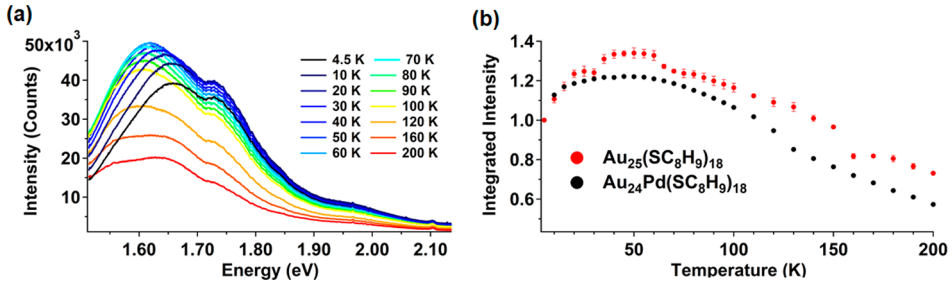

Figure 3. (a) PL spectra of $Au_{24}Pd(SC_8H_9)_{18}$ collected at sample temperatures of 4.5−200 K. (b) Temperature-dependent PL spectra integrated intensities of $Au_{25}(SC_8H_9)_{18}$ (red) and $Au_{24}Pd(SC_8H_9)_{18}$ (black).

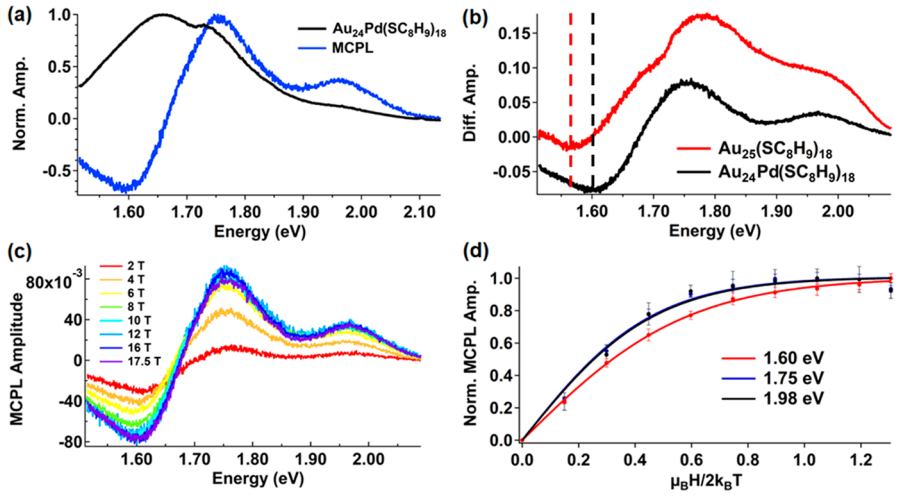

Figure 4. (a) PL Spectrum of $Au_{24}Pd(SC_8H_9)_{18}$ clusters (black) collected at 4.5 K overlaid with MCPL differential spectrum (blue) acquired at 17.5 T. (b) Comparison of MCPL differential spectra for $Au_{24}Pd(SC_8H_9)_{18}$ (black) and $Au_{25}(SC_8H_9)_{18}$ (red) acquired at sample temperatures of 4.5 K and field strengths of 17.5 T. The vertical dashed lines are guides to the eye that illustrate the blue-shifted emission of the $Au_{24}Pd(SC_8H_9)_{18}$ cluster. (c) Field-dependent MCPL spectra for $Au_{24}Pd(SC_8H_9)_{18}$ acquired at magnetic field strengths from 2T - 17.5 T. (d) MCPL magnetization curves for the 1.60 eV (red), 1.75 eV (blue), and 1.98 eV (black) emission acquired for multiple applied fields strengths at a sample temperature of 4.5 K. The solid lines represent fits using eq 3.

$$\mathrm{DOCP} = \frac{I_{\sigma^+} - I_{\sigma^-}}{I_{\sigma^+} + I_{\sigma^-}} \tag{1}$$

Here, I_{σ^+} and I_{σ^-} denote the magnetic field-induced intensity of left- and right-circularly polarized photoluminescence. We note that the experimental spectral range for this analysis is limited to energies greater than 1.55 eV by the polarization detection film. The DOCP spectrum for the $Au_{25}(SC_8H_9)_{18}$ cluster exhibits negligible amplitude at low energies (<1.63 eV) and increasing amplitude for higher energies (>1.63 eV). By comparison, the DOCP spectrum for $Au_{24}Pd(SC_8H_9)_{18}$ cluster exhibits more discrete character than observed for $Au_{25}(SC_8H_9)_{18}$. Specifically, the DOCP spectrum for the $Au_{24}Pd(SC_8H_9)_{18}$ exhibits two positive features centered at approximately 1.78 and 2.06 eV, and a negative amplitude feature less than 1.66 eV. The DOCP amplitudes for the $Au_{24}Pd(SC_8H_9)_{18}$ cluster at 1.78 and 2.06 eV were 0.07 and 0.18, respectively. The DOCP amplitudes for $Au_{25}(SC_8H_9)_{18}$ at these energies were 0.19 (1.78 eV) and 0.39 (2.06 eV), respectively. At low energies (<1.63 eV), the DOCP amplitude for the $Au_{24}Pd(SC_8H_9)_{18}$ cluster was approximately 0.05, whereas no DOCP amplitude was detected for the $Au_{25}(SC_8H_9)_{18}$. The observation of DOCP amplitude variations between $Au_{25}(SC_8H_9)_{18}$ and $Au_{24}Pd(SC_8H_9)_{18}$ clusters suggests the spin-character for radiative relaxation channels is modified upon Pd-atom substitution.

Temperature-Dependent PL Intensity. Previous studies have reported that PL intensity and energy dependent DOCP amplitude for the $Au_{25}(SC_8H_9)_{18}$ cluster is temperature dependent.[36] Figure 3a shows the PL spectra of $Au_{24}Pd(SC_8H_9)_{18}$ acquired at sample temperatures of 4.5−200 K. An increase in the PL yield is observed as sample temperature was increased from 4.5 to 40 K. Above 60 K, the integrated global PL intensity monotonically decreases with increasing temperature. This temperature-dependent integrated PL intensity behavior is shown for $Au_{24}Pd(SC_8H_9)_{18}$ in Figure 3b. A comparison for the previously reported temperature-dependent integrated intensities for the $Au_{25}(SC_8H_9)_{18}$ cluster is shown in red.[36,52] Interestingly, an increase in global PL intensity was observed for both clusters as sample temperatures were initially increased from 4.5 K. For the $Au_{25}(SC_8H_9)_{18}$, this temperature-dependent increase in PL intensity was assigned to thermally activated carrier transfer from a low-lying dark state to a higher energy radiative state.[36] Previously, the energy separation between bright and dark states was quantified using a two-level Boltzmann model given by eq 2

$$I(T) = \left(\frac{1}{\sqrt{T}}\right)\left(\frac{m + n\, e^{-\Delta/(k_B T)}}{1 + e^{-\Delta/(k_B T)}}\right) + A \tag{2}$$

Here, k_B is Boltzmann's constant, T is sample temperature, Δ is the energy separation, n and m are spectral weighting factors

https://doi.org/10.1021/acs.jpcc.1c00799
J. Phys. Chem. C 2021, 125, 7267−7275

for the bright and dark states, respectively, and A is a plateau function.[53] The activation barrier required to access the bright $Au_{25}(SC_8H_9)_{18}$ state was quantified as 3.3 ± 0.3 meV. A similar explanation likely applies to $Au_{24}Pd(SC_8H_9)_{18}$, for which we determined an activation barrier of 1.9 ± 0.1 meV. These observations indicate similar mechanisms for both MPCs, but that Pd substitution affects the electronic fine structure energies. The integrated intensity of the global PL for each cluster reached a maximum at approximately 50 K. The relative increase in PL intensity for $Au_{24}Pd(SC_8H_9)_{18}$ in going from 4.5 to 50 K is approximately half that observed for the $Au_{25}(SC_8H_9)_{18}$ cluster. This finding indicates that the bright emissive state is less efficient upon substitution by Pd into the Au_{13} core. Previous PL studies on $Ag_{25}(SC_8H_9)_{18}$ clusters similarly reported a decrease in global emission intensity upon Pd-doping.[54] To understand better both the decreased PL emission and energy-dependent DOCP observed upon Pd substitution, V$\vec{H}$-MCPL measurements were performed.

Variable-Field MCPL Analysis of $Au_{24}Pd(PET)_{18}$ Cluster. Magnetic circular photoluminescence spectroscopy was used to deconvolute the $Au_{24}Pd(SC_8H_9)_{18}$ global PL spectrum.[36,44,45] Figure 4a shows the $Au_{24}Pd(SC_8H_9)_{18}$ PL spectrum collected at 4.5 K overlaid with the MCPL spectrum acquired at 17.5 T applied field strength and 4.5 K. MCPL reveals three components for $Au_{24}Pd(SC_8H_9)_{18}$ global PL. The observation of the three differential PL components is in agreement with MCPL measurements on $Au_{25}(SC_8H_9)_{18}$.[36,44,45] Results from previous temperature-dependent PL and VT V$\vec{H}$-MCPL study of the $Au_{25}(SC_8H_9)_{18}$ cluster assigned the lowest energy component to metal−metal core-based intraband relaxation, whereas the two higher energy components were assigned to core-to-ligand interband relaxation. Figure 4b compares the MCPL spectra collected at 4.5 K and 17.5 T of $Au_{25}(SC_8H_9)_{18}$ and $Au_{24}Pd(SC_8H_9)_{18}$. The MCPL spectra for $Au_{25}(SC_8H_9)_{18}$ and $Au_{24}Pd(SC_8H_9)_{18}$ exhibit similar differential spectral profiles. A blue shift of the lower-energy component from 1.56 to 1.60 eV is observed for $Au_{24}Pd(SC_8H_9)_{18}$ when compared to $Au_{25}(SC_8H_9)_{18}$. However, this 40 meV blue shift does not solely account for the apparent 90-meV blue shifting observed for the global PL spectra of the two clusters. The global spectral blue shift is also the result of redistribution of the relative amplitudes of the PL components upon Pd substitution (Table 1). At 4.5 K, the percent contribution of the 1.60, 1.75, and 1.98 eV components were 32%, 57% and 11%, respectively, for $Au_{24}Pd(SC_8H_9)_{18}$. For $Au_{25}(SC_8H_9)_{18}$, the corresponding percentages were 59%, 36% and 5%. Therefore, the global PL intensity of the Pd-substituted cluster is shifted to higher energy because the more energetic transitions more significantly contribute to emission.

Based on our previous transition assignments for $Au_{25}(SC_8H_9)_{18}$ PL, the global blue shift of $Au_{24}Pd(SC_8H_9)_{18}$ corresponds to a relative increase in interband metal-to-ligand emission, with respect to intraband−metal−metal transitions, upon Pd substitution. The two higher energy MCPL components for the $Au_{24}Pd(SC_8H_9)_{18}$ cluster are centered at 1.75 and 1.98 eV. The 1.75 eV component exhibits a small red shift of approximately 20 meV compared to the corresponding $Au_{25}(SC_8H_9)_{18}$ feature centered at 1.77 eV. The highest energy MCPL component for each cluster is centered at 1.98 eV; the energy of this component is not affected by Pd substitution. This MCPL result, which shows that the low-energy emission of the MPC is sensitive to Pd substitution of an Au core atom, but the high-energy portion is not, validates our assignments of the low and high energy PL transitions to intraband and interband transitions, respectively.

Next, Landé g-factors are assigned to the three $Au_{24}Pd(SC_8H_9)_{18}$ PL components. Figure 4c shows the differential MCPL spectra for $Au_{24}Pd(SC_8H_9)_{18}$ obtained using a series of applied magnetic field strengths. The field-dependent VT V$\vec{H}$-MCPL amplitude for each component is plotted in Figure 4d. The Figure 4d data show strong similarity for the 1.75 and 1.98 eV components; the magnetic field dependence of the 1.60 eV PL peak is clearly distinct from emission at higher energy. To determine the Landé g-factor, which represents the angular momentum for each spin−orbit-coupled transition, field-dependent amplitudes were fit to eq 3[55]

$$\mathrm{MCPL} = A_{\mathrm{sat}} \tanh\left(\frac{g_J \mu_B \vec{H}}{2k_B T}\right) \tag{3}$$

Here, A_{sat} describes the point along the magnetization curve for which the MCPL intensity saturates, g_J is the Landé g-factor, μ_B is the Bohr magneton, and $\vec{H}$ is the applied field strength. Average g_J values and standard deviations from five trials for the 1.60, 1.75, and 1.98 eV components were 1.7 ± 0.1, 1.9 ± 0.1, and 1.9 ± 0.1, respectively. These values are all larger than those obtained for $Au_{25}(SC_8H_9)_{18}$ (Table 1).[36] The increased g_J values for $Au_{24}Pd(SC_8H_9)_{18}$ indicate that the substitution of Pd into the Au_{13} icosahedral core increases the total angular momenta of the emissive states. We previously showed that electron-vibrational coupling strengths increase with increasing Landé g-factors.[36] The increased vibrational coupling results in reduced emission yields because of increased contributions from nonradiative decay. The Figure 3b data, which show reduced integrated PL intensity upon Pd substitution, could result from a greater propensity for nonradiative decay due to increased angular momentum.

Electronic-Vibrational Coupling Analysis. To quantify the effect of electron-vibrational coupling on the three $Au_{24}Pd(SC_8H_9)_{18}$ PL transitions, the temperature-dependent emission intensity and energy of each component were analyzed. Figure 5a shows the temperature-dependent branching ratios for each PL component. As described above and in Table 1, 1.75 eV emission dominates the PL spectrum of $Au_{24}Pd(SC_8H_9)$ at 4.5 K, accounting for 57% of the total signal. As the sample temperature increases to 50 K, the relative amplitude of the 1.60 eV component increases and ultimately surpasses the amplitude of the 1.75 eV component, changing from 32% to 48% of the total signal. A similar, but

Table 1. PL Fit Values for $Au_{24}Pd(SC_8H_9)_{18}$ and $Au_{25}(SC_8H_9)_{18}$

component	energy (eV)	% (4.5 K)	% (50 K)	S	g_L
		$Au_{24}Pd(SC_8H_9)_{18}$			
1	1.60	32	48	5.3	1.7
2	1.75	57	43	9.3	1.9
3	1.98	11	9	9.3	1.9
		$Au_{25}(SC_8H_9)_{18}$			
1	1.56	59	74	4.0	1.1
2	1.77	36	24	9.0	1.6
3	1.98	5	2	4.8	1.05

https://doi.org/10.1021/acs.jpcc.1c00799
J. Phys. Chem. C 2021, 125, 7267−7275

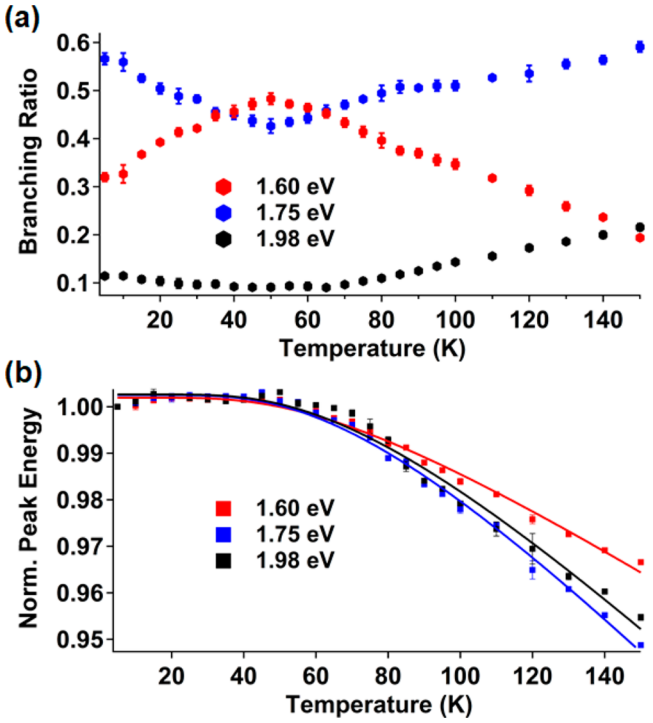

Figure 5. (a) Temperature-dependent branching ratios for individual PL components for the $Au_{24}Pd(SC_8H_9)_{18}$ cluster. (b) Normalized temperature-dependent peak energy shifts for each PL component.

more pronounced effect is observed for $Au_{25}(SC_8H_9)_{18}$. The low-energy emission component dominates global PL, but with an amplitude percentage of 74%. The cluster-dependent global PL temperature dependences (Figure 3b) are attributed to the smaller relative contribution of the 1.60 eV component emission upon Pd substitution. In general, the temperature-dependent branching ratio behavior of the 1.60 eV component mirrors the global integrated intensity. For sample temperatures greater than 50 K, the 1.75 eV component dominates the PL with increasing magnitude as the sample temperature is also increased.

Next, electron−phonon coupling constants for each PL component are quantified. Temperature-dependent PL energies were analyzed by the O'Donnell-Chen model (eq 4):[56]

$$E_g(T) = E_g(0) - S\hbar\omega\left[\coth\left(\frac{\hbar\omega}{2k_BT}\right) - 1\right] \quad (4)$$

$E_g(0)$ is the extrapolated peak energy at $T = 0$, S is a dimensionless coupling constant, $\hbar$ is Planck's constant, ω is the vibrational angular frequency, k_B is the Boltzmann constant, and T is the sample temperature. Figure 5b shows the normalized temperature-dependent peak energy shift for each PL component. After fitting the data to eq 4, average vibrational energy and coupling strength parameters were determined. Average vibrational energies of 18.4 ± 0.2, 20.8 ± 0.1, and 21.1. ± 0.4 meV (145 and 170 cm^{-1}) were quantified for the 1.60, 1.75, and 1.98 eV components, respectively. The vibrational energies for each component were within error of the values determined for the corresponding components of the $Au_{25}(SC_8H_9)_{18}$ cluster.[36] The 145 cm^{-1} vibrational mode for the 1.60 eV component agrees with a symmetric core-breathing mode.[57] The 170 cm^{-1} vibrational mode determined for the 1.75 and 1.98 eV components is attributed to Au−S stretching.[57,58] These assignments are consistent with core-based intraband transitions for the 1.60 eV component, and interband metal-to-ligand relaxation for the higher-energy emission. The results also indicate the three emission peaks are the same for both $Au_{25}(SC_8H_9)_{18}$ and $Au_{24}Pd(SC_8H_9)_{18}$. To understand the effect of the Pd-substitution on the spin-polarized PL of $Au_{25}(SC_8H_9)_{18}$ clusters, the nonradiative electron-vibrational and spin−orbit coupling constants were compared for both clusters.

Average and standard deviation values for vibrational coupling constants determined for the 1.60, 1.75, and 1.98 eV components were 5.3 ± 0.1, 9.3 ± 0.1, and 9.3 ± 0.2, respectively. Note, the similarity in S values for both interband transitions (1.75 and 1.98 eV) - and the unique value for the intraband one (1.60 eV) - support the assignments of the three PL components. The results also indicate that Au−S stretching results in stronger electron−phonon coupling than does core dilation. Figure 6 compares the vibrational coupling constants

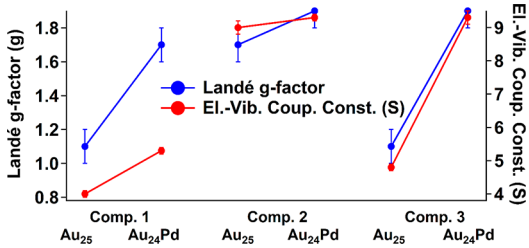

Figure 6. Comparison of Landé g-factors (blue) and el.-vib. coupling factors (red) for each PL component of $Au_{25}(SC_8H_9)_{18}$ and $Au_{24}Pd(SC_8H_9)_{18}$.

and Landé g-factors quantified for both $Au_{25}(SC_8H_9)_{18}$ and $Au_{24}Pd(SC_8H_9)_{18}$ clusters. For each PL component, an increase in the electron-vibrational coupling constant upon Pd substitution is observed. In general, when both clusters are considered, a larger Landé g-factor is accompanied by increases in electron−phonon coupling constants. The correlation between S and g_J can be generalized. Angular momentum must be conserved in the electronic relaxation process. Because the angular momentum carried by a photon (boson) is a fixed quantity, higher angular momentum transitions, such as those in $Au_{24}Pd(SC_8H_9)_{18}$ must rely on phonon modes for conservation. Hence, Pd substitution results in increased nonradiative, vibrationally mediated relaxation.

SUMMARY, DISCUSSION, AND CONCLUSIONS

The influence of Pd substitution on the photoluminescence properties of the $Au_{25}(SC_8H_9)_{18}$ cluster is reported. The Pd atom is known to replace an Au atom of the 13-atom icosahedral core of the cluster.[22] Qualitatively, the PL spectra spanning the range from 1.5 to 2.1 eV for $Au_{24}Pd(SC_8H_9)_{18}$ and $Au_{25}(SC_8H_9)_{18}$ are similar. PL spectra for both clusters consist of three emission components and show analogous temperature-dependent behavior; global PL intensity increases as sample temperature is raised from 4.5 K to approximately 50 K, but decreases as the sample temperature is elevated above 50 K. The qualitative similarities between the two clusters suggest that Pd substitution for gold in the $Au_{25}(SC_8H_9)_{18}$ core does not modify the PL mechanisms for these clusters. However, significant quantitative differences are observed for many properties upon Pd substitution. These properties include PL emission energies, degree of spin polarization,

https://doi.org/10.1021/acs.jpcc.1c00799
J. Phys. Chem. C 2021, 125, 7267−7275

Landé g-factors, and electron−phonon coupling strength, which collectively reflect increased propensity for nonradiative relaxation for the $Au_{24}Pd(SC_8H_9)_{18}$ species.

Comparison of the linear absorption spectra for $Au_{24}Pd(SC_8H_9)_{18}$ exhibited an energetic blue shift of approximately 130 meV, with respect to $Au_{25}(SC_8H_9)_{18}$, for transitions near the HOMO−LUMO energy gap. This absorption energy shift is explained by the conversion of the neutral seven-electron $Au_{25}(SC_8H_9)_{18}$ cluster to a six-electron superatom; incorporation of the valence-filled Pd atom to the central position of the icosahedral core modifies the cluster electron count.[22,25,29,39−41] For a six-electron superatom, the P_z orbital is unoccupied, resulting in an increased HOMO−LUMO energy gap.[22,25,29,39−41] The 4.5-K global PL spectrum of $Au_{24}Pd(SC_8H_9)_{18}$ was blue-shifted by approximately 60 meV, with respect to $Au_{25}(SC_8H_9)_{18}$. However, this blue shifting was the result of two separate effects: (1) transition-specific energy shifts and (2) differences in the relative amplitudes of the three resolvable radiative transitions. Therefore, the 90-meV global PL shift should not be correlated to a change in the energetics of any specific state. $Au_{24}Pd(SC_8H_9)_{18}$ exhibited a larger degree of spin polarization than $Au_{25}(SC_8H_9)_{18}$ at low emission energies (<1.66 eV). But spin polarization was larger for $Au_{25}(SC_8H_9)_{18}$ at energies exceeding 1.66 eV. To understand the complex PL spectra of the nanoclusters, each emission transition was analyzed using V$\vec{H}$-MCPL spectroscopy.

1.60 eV Emission. The 1.6 eV PL component of $Au_{24}Pd(SC_8H_9)_{18}$ is blue-shifted by 40 meV, with respect to the same peak for $Au_{25}(SC_8H_9)_{18}$. We previously assigned the $Au_{25}(SC_8H_9)_{18}$ peak to an excited $^2D_{5/2}$ to $^3P_{1/2}$ transition involving LUMO and HOMO states of the cluster core.[44,59] These terms were derived from V$\vec{H}$-MCPL magnetization curves. The observed 40-meV PL energy shift upon Pd substitution of a gold core atom is consistent with this assignment. Further supporting evidence of a core-based transition comes from vibrational mode analysis (Figure 5b), which shows that this transition is coupled to an acoustic breathing mode of the core. Interestingly, increased sample temperature increases—rather than reduces—the PL intensity. This temperature dependence is attributed to promotion of charge carriers from a dark to bright state, with the emissive state located 1.9 meV above the dark one. Aikens and coworkers have calculated the PL properties of several excited core states of a $Au_{25}(SR)_{18}$ series.[60] Incorporating energy corrections to account for differences in calculated and experimental emission energies, they conclude that PL in the range of 1.5−1.6 eV is most probable for relaxation from a manifold of states that include the fifth through seventh excited states and the HOMO, all of which are associated with the icosahedral core of the cluster.[60] Our experimental data agree well with the calculations from Aikens, and we attribute the 1.6 eV PL component to core-based transitions.

1.75 and 1.98 eV Emission. These transitions are more difficult to assign than the 1.6 eV component, and are grouped together because of their similar properties. On the basis of our previous VTV$\vec{H}$-MCPL studies of $Au_{25}(SC_8H_9)_{18}$, we detected mixing between core-based ^2D terms and ^4P states of the Au(I)-S ligand band manifold.[36,45] Both 1.75 and 1.98 eV transitions couple to Au(I)-S vibrations, which quench photoluminescence upon thermal activation. Au(I)-S stretching is a nonradiative relaxation channel for both the 1.75 and 1.98 eV transitions. Unfortunately, unambiguous term assignments could not be made for the $Au_{24}Pd(SC_8H_9)_{18}$ transitions, as was done for $Au_{25}(SC_8H_9)_{18}$. Landé g-factors of 1.9 are obtained for both 1.75 and 1.9 eV transitions, which are larger than the 1.7 value for the 1.6 eV transition. We note that the Landé g-factors are larger for all $Au_{24}Pd(SC_8H_9)_{18}$ transitions, with respect to the $Au_{25}(SC_8H_9)_{18}$ counterparts. As a result of increased angular momentum, electron−phonon coupling is stronger for the Pd-substituted clusters. One difference between the 1.75 and 1.98 eV peaks is that, while the higher energy component is not affected by Pd substitution (i.e., 1.98 eV for both $Au_{24}Pd(SC_8H_9)_{18}$ and $Au_{25}(SC_8H_9)_{18}$), the lower energy one exhibits a 30-meV red shift. Therefore, we attribute the properties of these two higher energy components to mixing between core and ligand band states. We note that the calculations from Aikens did not extend to PL emission energies as high as these two components.[60]

The global PL properties of the MPCs were the result of transition-specific emission. For both clusters, an increase in the global integrated intensity was observed as sample temperatures increased from 4.5 to 50 K, which was correlated to intraband metal−metal emission by core-based states. In the low-temperature regime ($T \leq 50$ K) emission for both MPCs was dominated by core-based states. However, for sample temperatures exceeding 50 K, emission preceded by a manifold of states that were likely derived from a mixture of metal core atom and metal sulfide-based levels. We previously quantified temperature- and magnetic-field-dependent photoluminescence lifetimes of $Au_{25}(SC_8H_9)_{18}$.[44] These studies revealed two emission lifetimes: (i) $\tau_1 \approx 50$ μs and (ii) $\tau_2 \approx 160$ μs. An important correlation between our VTV$\vec{H}$-MCPL and time-resolved results is that the Arrhenius analysis of the PL time constants yields thermal activation barriers of approximately 610 μeV for τ_1 and τ_2, respectively.[44] These energy barriers are comparable to the several hundred micro-eV barriers obtained for the 1.75 and 1.98 eV peaks using VTV$\vec{H}$-MCPL analysis.[36] Therefore, we conclude that the PL lifetimes reflect the emission of the 1.75 and 1.98 eV peaks. Goodson and coworkers detected ultrafast (i.e., hundreds of femtosecond) visible emission for similar MPCs.[61] This short time scale is beyond the picosecond instrumental resolution of our photon-counting system, and may explain why a third PL lifetime associated with metal−metal 1.6 eV emission is not detected.

An observation that was general across all transitions and for both clusters is that the electron-vibrational coupling strength was directly related to spin−orbit coupling (i.e., proportional to the Landé g_J factor) for each radiative transition. Notably, the increase in electron-vibrational constant, S, and g_J of the intraband metal−metal transitions resulting from Pd substitution was approximately 55% and 30%, respectively. By comparison, the increases in S and g_J for the mixed metal−ligand states were much smaller upon Pd substitution—19% and 3%, respectively. This observation is rationalized based on the peak assignments: Pd substitution of the Au_{13} core has a much larger influence on metal−metal transitions than on those associated with the ligand band. On the basis of temperature-dependent integrated global PL intensity and branching ratio analysis, the increase in electron-vibrational coupling of the intraband core-based emission channel upon Pd-doping results in reduced emission by the 25-metal-atom cluster. The decrease in global emission intensity is correlated

https://doi.org/10.1021/acs.jpcc.1c00799
J. Phys. Chem. C 2021, 125, 7267−7275

to a greater partitioning of carrier relaxation to nonradiative channels due to stronger vibrational coupling.

The results indicate that atomic substitution in structurally well-defined clusters can lead to large changes in the optical and spin-dependent properties of MPCs. These structural effects can be linked to specific radiative transition through state-resolved spectroscopy. The ability to correlate atomic-level structure to specific optical responses can lead to predictive development of functional photonic materials. Despite these advances, the emission properties of metal nanoclusters are clearly complex.[62,63] The multiple, discrete emission peaks observed here deviate from those typical of molecules or semiconducting nanoparticles.[64,65] Therefore, MPC systems provide exciting opportunities to study unique fundamental photophysics, and to structurally tailor the optical properties of colloidal materials.

AUTHOR INFORMATION

Corresponding Author

Kenneth L. Knappenberger, Jr. − *Department of Chemistry, The Pennsylvania University, University Park, Pennsylvania 16802, United States;* orcid.org/0000-0003-4123-3663; Email: klk260@psu.edu

Authors

Patrick J. Herbert − *Department of Chemistry, The Pennsylvania University, University Park, Pennsylvania 16802, United States*

Marcus A. Tofanelli − *Department of Chemistry, Colorado State University, Fort Collins, Colorado 80523, United States*

Christopher J. Ackerson − *Department of Chemistry, Colorado State University, Fort Collins, Colorado 80523, United States;* orcid.org/0000-0001-6863-6054

Complete contact information is available at: https://pubs.acs.org/10.1021/acs.jpcc.1c00799

Notes

The authors declare no competing financial interest.

ACKNOWLEDGMENTS

This work was supported by awards from the National Science Foundation to K.L.K., under Grant No. CHE-1806222/CHE-1904876 and CHE-1807999. In addition, this work was supported by awards from the National Science Foundation to C.J.A. under Grant Nos. CHE-1905179 and CHE-1507646.

REFERENCES

(1) Jadzinsky, P. D.; Calero, G.; Ackerson, C. J.; Bushnell, D. A.; Kornberg, R. D. Structure of a Thiol Monolayer-Protected Gold Nanoparticle at 1.1 Å Resolution. *Science* **2007**, *318*, 430−433.

(2) Li, G.; Jin, R. Atomically Precise Gold Nanoclusters as New Model Catalysts. *Acc. Chem. Res.* **2013**, *46*, 1749−1758.

(3) Knoppe, S.; Vanbel, M.; van Cleuvenbergen, S.; Vanpraet, L.; Bürgi, T.; Verbiest, T. Nonlinear Optical Properties of Thiolate-Protected Gold Clusters. *J. Phys. Chem. C* **2015**, *119*, 6221−6226.

(4) Negishi, Y.; Kurashige, W.; Niihori, Y.; Nobusada, K. Toward the Creation of Stable, Functionalized Metal Clusters. *Phys. Chem. Chem. Phys.* **2013**, *15*, 18736−18751.

(5) Kang, X.; Chong, H.; Zhu, M. $Au_{25}(SR)_{18}$: The Captain of the Great Nanocluster Ship. *Nanoscale* **2018**, *10*, 10758−10834.

(6) Yi, C.; Zheng, H.; Herbert, P. J.; Chen, Y.; Jin, R.; Knappenberger, K. L. Ligand- and Solvent-Dependent Electronic Relaxation Dynamics of $Au_{25}(SR)_{18}^{-}$ Monolayer-Protected Clusters. *J. Phys. Chem. C* **2017**, *121*, 24894−24902.

(7) Zhu, M.; Aikens, C. M.; Hollander, F. J.; Schatz, G. C.; Jin, R. Correlating the Crystal Structure of A Thiol-Protected Au_{25} Cluster and Optical Properties. *J. Am. Chem. Soc.* **2008**, *130*, 5883−5885.

(8) Kurashige, W.; Yamaguchi, M.; Nobusada, K.; Negishi, Y. Ligand-Induced Stability of Gold Nanoclusters: Thiolate versus Selenolate. *J. Phys. Chem. Lett.* **2012**, *3*, 2649−2652.

(9) Shichibu, Y.; Negishi, Y.; Watanebe, T.; Chaki, N. K.; Kawaguchi, H.; Tsukuda, T. Biicosahedral Gold Clusters $[Au_{25}(PPh_3)_{10}(SC_nH_{2n+1})_5Cl_2]^{2+}$ (n = 2−18): A Stepping Stone to Cluster-Assembled Materials. *J. Phys. Chem. C* **2007**, *111*, 7845−7847.

(10) Kurashige, W.; Yamazoe, S.; Yamaguchi, M.; Nishido, K.; Nobusada, K.; Tsukuda, T.; Negishi, Y. Ligand Exchange Reactions in Thiolate-Protected Au_{25} Nanoclusters with Selenolates or Tellurolates: Preferential Exchange Sites and Effects on Electronic Structure. *J. Phys. Chem. Lett.* **2014**, *5*, 2072−2076.

(11) Sels, A.; Barrabés, N.; Knoppe, S.; Bürgi, T. Isolation of Atomically Precise Mixed Ligand Shell $PdAu_{24}$ Clusters. *Nanoscale* **2016**, *8*, 11130−11135.

(12) Jin, R.; Nobusada, K. Doping and Alloying in Atomically Precise Gold Nanoparticles. *Nano Res.* **2014**, *7*, 285−300.

(13) Ghosh, A.; Mohammed, O. F.; Bakr, O. M. Atomic-Level Doping of Metal Clusters. *Acc. Chem. Res.* **2018**, *51*, 3094−3103.

(14) Niihori, Y.; Kurashige, W.; Matsuzaki, M.; Negishi, Y. Remarkable Enhancement in Ligand-Exchange Reactivity of Thiolate-Protected Au_{25} Nanocluster by Single Pd Atom Doping. *Nanoscale* **2013**, *5*, 508−512.

(15) Guidez, E. B.; Mäkinen, V.; Häkkinen, H.; Aikens, C. M. Effects of Silver Doping on the Geometric and Electronic Structure and Optical Absorption Spectra of the $Au_{25-n}Ag_n(SH)_{18}^{-}$ (n = 1, 2, 4, 6, 8, 10, 12) Bimetallic Nanoclusters. *J. Phys. Chem. C* **2012**, *116*, 20617−20624.

(16) Zheng, H.; Tofanelli, M. A.; Ackerson, C. J.; Knappenberger, K. L. Composition-Dependent Electronic Energy Relaxation Dynamics of Metal Domains as Revealed by Bimetallic $Au_{144-x}Ag_x(SC_8H_9)_{60}$ Monolayer-Protected Clusters. *Phys. Chem. Chem. Phys.* **2017**, *19*, 14471−14477.

(17) Hartmann, M. J.; Häkkinen, H.; Millstone, J. E.; Lambrecht, D. S. Impacts of Copper Position on the Electronic Structure of $[Au_{25-x}Cu_x(SH)_{18}]^{-}$ Nanoclusters. *J. Phys. Chem. C* **2015**, *119*, 8290−8298.

(18) Sharma, S.; Yamazoe, S.; Ono, T.; Kurashige, W.; Niihori, Y.; Nobusada, K.; Tsukuda, T.; Negishi, Y. Tuning the Electronic Structure of Thiolate-Protected 25-Atom Clusters by co-Substitution with Metals Having Different Preferential Sites. *Dalton Trans.* **2016**, *45*, 18064−18068.

(19) Sharma, S.; Kurashige, W.; Nobusada, K.; Negishi, Y. Effect of Trimetallization in Thiolate-Protected $Au_{24-n}Cu_nPd$ Clusters. *Nanoscale* **2015**, *7*, 10606−10612.

(20) Wang, S.; Meng, X.; Das, A.; Li, T.; Song, Y.; Cau, T.; Zhu, X.; Zhu, M.; Jin, R. A 200-fold Quantum Yield Boost in the Photoluminescence of Silver Doped Ag_xAu_{25-x} Nanoclusters: The 13th Silver Atom Matters. *Angewandte Comm.* **2014**, *53*, 2376−2380.

(21) Qian, H.; Jiang, D.; Li, G.; Gayathri, C.; Das, A.; Gil, R. R.; Jin, R. Monoplatinum Doping of Gold Nanoclusters and Catalytic Application. *J. Am. Chem. Soc.* **2012**, *134*, 16159−16162.

(22) Tofanelli, M. A.; Ni, T. W.; Phillips, B. D.; Ackerson, C. J. Crystal Structure of the $PdAu_{24}(SR)_{18}^{0}$ Superatom. *Inorg. Chem.* **2016**, *55*, 999−1001.

(23) Jiang, D.; Dai, S. From Superatomic $Au_{25}(SR)_{18}^{-}$ to Superatomic $M@Au_{24}(SR)_{18}^{q}$ Core-Shell Clusters. *Inorg. Chem.* **2009**, *48*, 2720−2722.

(24) Walter, M.; Moseler, M. Ligand-Protected Gold Alloy Clusters: Doping the Superatom. *J. Phys. Chem. C* **2009**, *113*, 15834−15837.

(25) Kwak, K.; Tang, Q.; Kim, M.; Jiang, D.; Lee, D. Interconversion Between Superatomic 6-Electron and 8-Electron Configurations of $M@Au_{24}(SR)_{18}$ Clusters (M = Pd, Pt). *J. Am. Chem. Soc.* **2015**, *137*, 10833−10840.

(26) Tian, S.; Liao, L.; Yuan, J.; Yao, C.; Chen, J.; Yang, J.; Wu, Z. Structures and Magnetism of Mono-Palladium and Mono-Platinum

Doped $Au_{25}(PET)_{18}$ Nanoclusters. *Chem. Commun.* **2016**, *52*, 9873−9876.
(27) Li, Y.; Biswas, S.; Luo, T.-Y.; Juarez-Mosqueda, R.; Taylor, M. G.; Mpourmpakis, G.; Rosi, N. L.; Hendrich, M. P.; Jin, R. Doping Effect on the Magnetism of Thiolate-Capped 25-Atom Alloy Nanoclusters. *Chem. Mater.* **2020**, *32*, 9238−9244.
(28) Zhou, M.; Qian, H.; Sfeir, M. Y.; Nobusada, K.; Jin, R. Effects of Single Atom Doping on the Ultrafast Electron Dynamics of $M_1Au_{24}(SR)_{18}$ (M = Pd, Pt) Nanoclusters. *Nanoscale* **2016**, *8*, 7163−7171.
(29) Williams, L. J.; Herbert, P. J.; Tofanelli, M. A.; Ackerson, C. J.; Knappenberger, K. L. Superatom Spin-State Dynamics of Structurally Precise Metal Monolayer-Protected Clusters (MPCs). *J. Chem. Phys.* **2019**, *150*, 101102−7.
(30) Zhu, M.; Aikens, C. M.; Hendrich, M. P.; Gupta, R.; Qian, H.; Schatz, G. C.; Jin, R. Reversible Switching of Magnetism in Thiolate-Protected Au Superatoms. *J. Am. Chem. Soc.* **2009**, *131*, 2490−2492.
(31) McCoy, R. S.; Choi, S.; Collins, G.; Ackerson, B. J.; Ackerson, C. J. Superatom Paramagnetism Enables Gold Nanocluster Heating in Applied Radiofrequency Fields. *ACS Nano* **2013**, *7*, 2610−2616.
(32) Tofanelli, M. A.; Salorinne, K.; Ni, T. W.; Malola, S.; Newell, B.; Phillips, B.; Häkkinen, H.; Ackerson, C. J. Jahn-Teller Effects in $Au_{25}(SR)_{18}$. *Chem. Sci.* **2016**, *7*, 1882−1890.
(33) Jena, P.; Castleman, A. W. Clusters: A Bridge Across the Disciplines of Physics and Chemistry. *Proc. Natl. Acad. Sci. U. S. A.* **2006**, *103*, 10560−10569.
(34) Castleman, A. W.; Harms, A. C.; Leuchtner, Z. Gas Phase Reactivity of Thermal Metal Clusters. *Z. Phys. D: At., Mol. Clusters* **1991**, *19*, 343−34.
(35) Walter, M.; Akola, J.; Lopez-Acevedo, O.; Jadzinsky, P. D.; Calero, G.; Ackerson, C. J.; Whetten, R. L.; Grönbeck, H.; Häkkinen, H. A Unified View of Ligand-Protected Gold Clusters as Superatom Complexes. *Proc. Natl. Acad. Sci. U. S. A.* **2008**, *105*, 9157−9162.
(36) Herbert, P. J.; Knappenberger, K. L. Spin-Polarized Photoluminescence in $Au_{25}(SC_8H_9)_{18}$ Monolayer-Protected Clusters. *Small* **2021**, 2004431.
(37) Agrachev, M.; Antonello, S.; Dainese, T.; Ruzzi, M.; Zoleo, A.; Aprá, E.; Govind, N.; Fortunelli, A.; Sementa, L.; Maran, F. Magnetic Ordering in Gold Nanoclusters. *ACS Omega* **2017**, *2*, 2607−2617.
(38) Negishi, Y.; Kurashige, W.; Niihori, Y.; Iwasa, T.; Nobusada, K. Isolation, Structure, and Stability of a Dodecanethiolate-Protected Pd_1Au_{24} Cluster. *Phys. Chem. Chem. Phys.* **2010**, *12*, 6219−6225.
(39) Kacprzak, K. A.; Lehtovaara, L.; Akola, J.; Lopez-Acevedo, O.; Häkkinen, H. A Density Functional Investigation of Thiolate-Protected Bimetal $PdAu_{24}(SR)_{18}^{z}$ Clusters: Doping the Superatom Complex. *Phys. Chem. Chem. Phys.* **2009**, *11*, 7123−7129.
(40) Yan, J.; Su, H.; Yang, H.; Malola, S.; Lin, S.; Häkkinen, H.; Zheng, N. Total Structure and Electronic Structure Analysis of Doped Thiolated Silver $[MAg_{24}(SR)_{18}]^{-2}$ (M = Pd, Pt) Clusters. *J. Am. Chem. Soc.* **2015**, *137*, 11880−11883.
(41) Alkan, F.; Pandeya, P.; Aikens, C. M. Understanding the Effect of Doping on Energetics and Electronic Structure for Au_{25}, Ag_{25}, and Au_{38} Clusters. *J. Phys. Chem. C* **2019**, *123*, 9516−9527.
(42) Negishi, Y.; Kurashige, W.; Kobayashi, Y.; Yamazoe, S.; Kojima, N.; Seto, M.; Tsukuda, T. Formation of a $Pd@Au_{12}$ Superatomic Core in $Au_{24}Pd_1(SC_{12}H_{25})_{18}$ Probed by ^{197}Au Mössbauer and Pd K-Edge EXAFS Spectroscopy. *J. Phys. Chem. Lett.* **2013**, *4*, 3579−3583.
(43) Fei, W.; Antonello, S.; Dainese, T.; Dolmella, A.; Lahtinen, M.; Rissanen, K.; Venzo, A.; Maran, F. Metal Doping of $Au_{25}(SR)_{18}^{-}$ Clusters: Insights and Hindsights. *J. Am. Chem. Soc.* **2019**, *141*, 16033−16045.
(44) Green, T. D.; Herbert, P. J.; Yi, C.; Zeng, C.; McGill, S.; Jin, R.; Knappenberger, K. L. Characterization of Emissive State for Structurally Precise $Au_{25}(SC_8H_9)_{18}^{0}$ Monolayer-Protected Gold Nanoclusters Using Magnetophotoluminescence Spectroscopy. *J. Phys. Chem. C* **2016**, *120*, 17784−17790.
(45) Herbert, P. J.; Mitra, U.; Knappenberger, K. L. Variable-Temperature Variable-Field Magnetic Circular Photoluminescence (VTVH-MCPL) Spectroscopy for Electronic-Structure Determination in Nanoscale Chemical Systems. *Opt. Lett.* **2017**, *42*, 4833−4836.
(46) Herbert, P. J.; Window, P.; Ackerson, C. J.; Knappenberger, K. L. Low-Temperature Magnetism in Nanoscale Gold Revealed through Variable-Temperature Magnetic Circular Dichroism Spectroscopy. *J. Phys. Chem. Lett.* **2019**, *10*, 189−193.
(47) Aikens, C. M. Electronic Structure of Ligand-Passivated Gold and Silver Nanoclusters. *J. Phys. Chem. Lett.* **2011**, *2*, 99−104.
(48) Aikens, C. Electronic and Geometric Structure, Optical Properties, and Excited State Behavior in Atomically Precise Thiolate-Stabilized Noble Metal. *Acc. Chem. Res.* **2018**, *51*, 3065−3073.
(49) Jin, R.; Qian, H.; Wu, Z.; Zhu, Y.; Zhu, M.; Mohanty, A.; Garg, N. Size Focusing: A Methodology for Synthesizing Atomically Precise Gold Nanoclusters. *J. Phys. Chem. Lett.* **2010**, *1*, 2903−2910.
(50) Tofanelli, M. A.; Ackerson, C. J. Superatom Electron Configuration Predicts Thermal Stability of $Au_{25}(SR)_{18}$ Nanoclusters. *J. Am. Chem. Soc.* **2012**, *134*, 16937−16940.
(51) Jiang, D.; Kühn, M.; Tang, Q.; Weigend, F. Superatomic Orbitals under Spin-Orbit Coupling. *J. Phys. Chem. Lett.* **2014**, *5*, 3286−3289.
(52) Green, T. D.; Yi, C.; Zeng, C.; Jin, R.; McGill, S.; Knappenberger, K. L., Jr. Temperature-Dependent Photoluminescence of Structurally-Precise Quantum-Confined $Au_{25}(SC_8H_9)_{18}$ and $Au_{38}(SC_{12}H_{25})_{24}$ Metal Nanoparticles. *J. Phys. Chem. A* **2014**, *118*, 10611−10621.
(53) Mortimer, I. B.; Nicholas, R. J. Role of Bright and Dark Excitons in the Temperature-Dependent Photoluminescence of Carbon Nanotubes. *Phys. Rev. Lett.* **2007**, *98*, 027404.
(54) Liu, X.; Yuan, J.; Yao, C.; Chen, J.; Li, L.; Bao, X.; Yang, J.; Wu, Z. Crystal and Solution Photoluminescence of $MAg_{24}(SR)_{18}$ (M = Ag/Pd/Pt/Au) Nanoclusters and Some Implications for the Photoluminescence Mechanisms. *J. Phys. Chem. C* **2017**, *121*, 13848−13853.
(55) Stephens, P. J. Magnetic Circular Dichroism. *Adv. Chem. Phys.* **1976**, *35*, 197−264.
(56) O'Donnell, K. P.; Chen, X. Temperature Dependence of Semiconductor Band Gaps. *Appl. Phys. Lett.* **1991**, *54*, 2924−2926.
(57) Tlahuice-Flores, A. Normal Modes of $Au_{25}(SCH_3)_{18}^{-}$, $Ag_{12}Au_{13}(SCH_3)_{18}^{-}$ and $Ag_{25}(SCH_3)_{18}^{-}$ Clusters. *Mol. Simul.* **2013**, *39*, 428−431.
(58) Parker, J. F.; Choi, J. P.; Wang, W.; Murray, R. W. Electron Self-Exchange Dynamics of the Nanoparticle Couple $[Au_{25}(SC_2Ph)_{18}]^{0/-1}$ By Nuclear Magnetic Resonance Line-Broadening. *J. Phys. Chem. C* **2008**, *112*, 13976−13981.
(59) Zhao, T.; Herbert, P. J.; Zheng, H.; Knappenberger, K. L. State-Resolved Metal Nanoparticle Dynamics Viewed through the Combined Lenses of Ultrafast and Magneto-optical Spectroscopies. *Acc. Chem. Res.* **2018**, *51*, 1433−1442.
(60) Weerawardene, K. L. D. M.; Aikens, C. M. Theoretical Insights into the Origin of Photoluminescence of $Au_{25}(SR)_{18}^{-}$ Nanoparticles. *J. Am. Chem. Soc.* **2016**, *138*, 11202−11210.
(61) Yau, S. H.; Varnavski, O.; Gilberston, J. D.; Chandler, B.; Ramakrishna, G.; Goodson, T. Ultrafast Optical Study of Small Gold Monolayer Protected Clusters: A Closer Look at Emission. *J. Phys. Chem. C* **2010**, *114*, 15979−15985.
(62) Kang, Xi; Zhu, M. Tailoring the Photoluminescence of Atomically Precise Nanoclusters. *Chem. Soc. Rev.* **2019**, *48*, 2422−2457.
(63) Yang, J.; Jin, R. Advances in Enhancing Luminescence of Atomically Precise Ag Clusters. *J. Phys. Chem. C* **2021**, *125*, 2619−2625.
(64) Kasha, M. Characterization of Electronic Transitions in Complex Molecules. *Discuss. Faraday Soc.* **1950**, *9*, 14−19.
(65) Murray, C. B.; Kagan, C. R.; Bawendi, M. G. Synthesis and Characterization of Monodispersed Nanocrystals and Close-Packed Nanocrystal Assemblies. *Annu. Rev. Mater. Sci.* **2000**, *30*, 545−610.

https://doi.org/10.1021/acs.jpcc.1c00799
J. Phys. Chem. C 2021, 125, 7267−7275